

Stability and Resolution Analysis of a Phase-Locked Loop Natural Frequency Tracking System for MEMS Fatigue Testing

X. Sun
Graduate Student

R. Horowitz
Professor

K. Komvopoulos
Professor
Fellow ASME

Department of Mechanical Engineering,
University of California,
Berkeley, CA 94720

An analysis of a nonlinear control system that was used to track the natural frequency of a MEMS resonator is presented in this paper. A phase-locked loop system is used to track the natural frequency of the resonator due to fatigue of the spring element. A model for the control system is established and the system behavior is analyzed using an averaging method. The analysis provides a quantitative criterion for selecting the control gain to achieve stability. Simulation results are shown to be in agreement with the theoretical analysis. Tracking accuracy under the presence of Brownian noise and capacitive position sensing noise is also analyzed by using a variance propagation equation for the nonlinear dynamic system utilizing a first-order Taylor series approximation. The theoretically estimated resolution is also found to be in good agreement with simulation results.

[DOI: 10.1115/1.1514658]

1 Introduction

Natural frequency tracking is a frequently encountered task in controlling microelectromechanical system (MEMS) devices. For example, vibratory rate sensors, such as MEMS gyroscopes, must be excited at their natural frequencies, which often shift due to temperature sensitivity. Of particular significance is the capability to track the natural frequency decay of an oscillating MEMS device due to the decrease of the stiffness of spring elements resulting mainly from fatigue damage. As in macroscopic mechanical devices, fatigue is also an important phenomenon in miniature devices like MEMS resonators. Understanding of the fatigue mechanism of MEMS structural materials is of great importance in reliability analysis of MEMS devices and influences micromachine operation and robustness. However, fatigue damage at the microscale has attracted the attention of researchers only recently.

To investigate fatigue under cyclic loading in MEMS devices, a two-layer polycrystalline silicon resonator [1], such as that shown in Fig. 1, was fabricated using the MUMPS process [2]. The beams in the middle of the device, attached to an anchor and a rotating ring, are the test samples (fatigue specimens). These flexure beams bend when the shutters (i.e., the moving elements of the resonator) of the comb drives rotate, and function as the suspension of the resonator. The comb drives are divided into two groups, marked by *A* and *B* in Fig. 1, respectively, and the comb drives in each group are electrically connected via the two rings around the device. Group *A* of the comb drives is used to generate electrostatic forces that excite the resonator, while group *B* is used to sense the position of the shutter by measuring the capacitance change caused by displacement.

Tracking the natural frequency during fatigue testing is crucial for the following reasons:

1. Large strains in the test samples can only be achieved at resonance. The MEMS resonators are lightly damped and have high quality factors Q (~ 100 in air and in the range of $10^4 - 10^5$ in vacuum). Thus, the large displacements needed

to produce sufficient deformation can only be achieved at resonance, i.e., at a frequency very close to the natural frequency of a lightly damped system.

2. The natural frequency decay is used to determine the change of the stiffness of the test samples due to the evolution of fatigue damage. During cyclic loading, grains in the test samples may be damaged, causing the effective stiffness to decrease, and, in turn, the natural frequency of the resonator to decay. Therefore, the characteristics of the fatigue process can be studied by observing the evolution of the natural frequency.

Phase-locked loops (PLLs) have been previously used to track the natural frequency of a vibrating resonator in MEMS fatigue testing experiments [3–5]. However, rigorous analysis of the stability and performance of this control scheme has not been reported in the literature. The principal objective of this study, therefore, is to quantitatively analyze the stability and resolution of this PLL control scheme. A fifth-order nonlinear dynamic model of the entire system including the PLL, resonator, and driving and sensing circuits is presented, and the nonlinear dynamic system is examined by developing a simplified (although still nonlinear) system of dynamic equations. It is demonstrated that excitation at the natural frequency yields a stable closed orbit of the original system, provided a certain criterion for the control gain is satisfied. Simulation results for the original system that verify the validity of the analysis are discussed, and the tracking accuracy under the presence of Brownian noise and capacitive position sensing noise is interpreted in light of the obtained results. The tracking resolution is estimated by approximating the nonlinear variance propagation equation by a first-order Taylor series. The natural frequency tracking resolution at steady state is obtained by solving a Lyapunov equation.

2 Phase-Locked Loop and System Model

A PLL consists of three functional blocks: phase detector, controller, and voltage-controlled oscillator (VCO), as illustrated in Fig. 2. The phase detector compares the phase difference between the reference and the output, and feeds the error signal, which is proportional to the phase difference, to the controller. From this error signal, the controller calculates the control voltage of the VCO, and the oscillating frequency of the VCO is an affine func-

Contributed by the Dynamic Systems and Control Division of THE AMERICAN SOCIETY OF MECHANICAL ENGINEERS for publication in the ASME JOURNAL OF DYNAMIC SYSTEMS, MEASUREMENT, AND CONTROL. Manuscript received by the ASME Dynamic Systems and Control Division, August 2001; final revision, March 2002. Associate Editor: M. Goldfarb.

tion of this control voltage in the operating range. Thus, with a proper design of the controller, the output of the PLL can track the reference signal in both frequency and phase. Details regarding the operating principles of PLL can be found in Ref. [6].

For an analog PLL, a four-quadrant multiplier and a low-pass filter are often used as the phase detector, as in the system of this study. The block diagram of the entire system is shown in Fig. 3. The output of the PLL is first amplified and then fed to the driving combs of the resonator. The position of the resonator is measured by capacitive sensing circuits. The phase difference between the measured position signal and the excitation signal, which is the output of the VCO, is compared by the phase detector. The control voltage of the VCO is calculated by the controller from this phase difference. The equations describing the behaviors of these functional blocks are established next.

The resonator is modeled as a second-order spring-mass-damper system with a dynamic behavior described by

$$\ddot{x} + c\dot{x} + \omega_n^2 x = F, \quad (1)$$

where x is the position, c is the normalized damping factor, ω_n is the natural frequency, and F is the normalized driving force. The driving force is an electrostatic force generated by the comb drives and can be derived from the electrical potential energy stored in the capacitance of the comb drives. Assuming a parallel-plate model for the comb drive capacitance, C ,

$$C = \epsilon \frac{tl}{d}, \quad (2)$$

where ϵ is the permittivity, t is the thickness of the comb fingers, l is the overlap length of the fingers, and d is the width of the gap between fingers, the electrical potential energy stored in the capacitance, U , can be written as

$$U = \frac{1}{2} CV^2 = \frac{\epsilon tl}{2d} V^2, \quad (3)$$

where V is the voltage applied across the comb fingers. For lateral comb drives used in this study, the electrostatic force, F , is obtained as

$$F = -\frac{\partial U}{\partial l} = -\frac{\epsilon t}{2d} V^2, \quad (4)$$

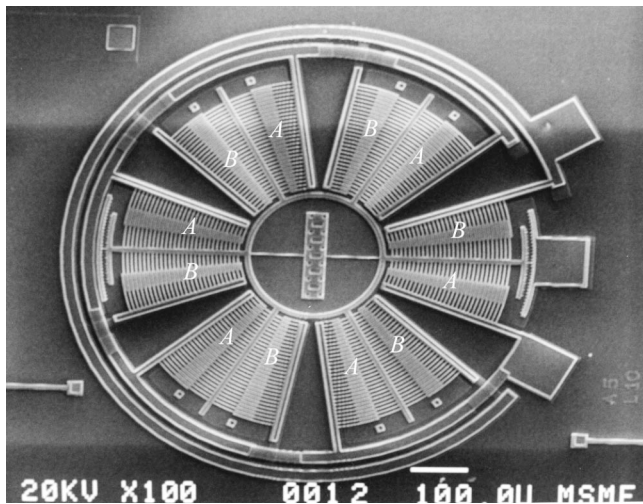


Fig. 1 Scanning electron microscopy image of a polycrystalline silicon MEMS resonator used for fatigue testing.

i.e., the electrostatic force is proportional to the voltage squared. The applied voltage usually consists of two components—a DC bias voltage V_{bias} and an AC driving voltage $V_{\text{dr}} \cos \omega t$. Thus, the squared voltage is given by

$$V^2 = (V_{\text{bias}} + V_{\text{dr}} \cos \omega t)^2 = V_{\text{bias}}^2 + 2V_{\text{bias}} V_{\text{dr}} \cos \omega t + V_{\text{dr}}^2 \cos^2 \omega t. \quad (5)$$

The first term of Eq. (5) is a constant and does not contribute to the oscillating driving force. Since the amplitude of the AC driving voltage is chosen to be much smaller than the bias voltage, the third term of Eq. (5) is much smaller than the second term and can be neglected. Therefore, under proper bias, the driving force is approximately proportional to the AC driving voltage, which is the amplified VCO output.

The driving force can be written as

$$F = A \cos \theta, \quad (6)$$

where $\cos \theta$ is the output of the VCO, θ is the instantaneous phase, and A is the amplitude of the force, which is the product of the gain of the driving amplifier and the hardware gain (from voltage to force) of the comb drives.

From the architecture of the VCO, the instantaneous frequency, ω , is an affine function of the control voltage, z , and is written as

$$\omega := \dot{\theta} = \omega_0 + K_{\text{VCO}} z, \quad (7)$$

where ω_0 is the free oscillation frequency. The instantaneous phase of the VCO is thus the integral of the instantaneous frequency

$$\theta = \int_0^t (\omega_0 + K_{\text{VCO}} z) d\tau. \quad (8)$$

The control voltage of the VCO is calculated from the output of the phase detector, y , by an integral controller,

$$z = K_I \int_0^t y d\tau,$$

i.e.,

$$\dot{z} = K_I y, \quad (9)$$

where K_I is the integral control gain. The output of the phase detector is the product of the measured position signal, $K_G x$, and the VCO output, $\cos \theta$, filtered by a low-pass filter, i.e.,

$$\dot{y} = \lambda (K_G x \cos \theta - y), \quad (10)$$

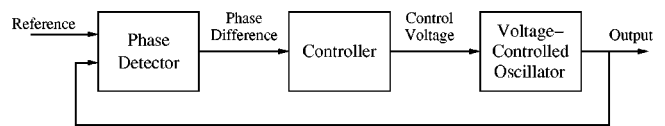


Fig. 2 Block diagram of a phase-locked loop.

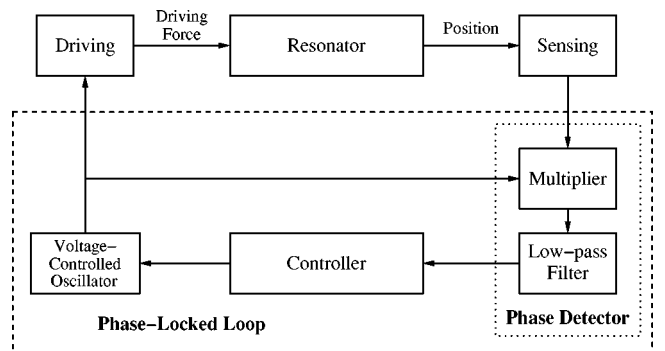


Fig. 3 Block diagram of the natural frequency tracking system for a MEMS resonator.

where K_G is the gauge factor (from position to voltage) of the sensing combs and circuits, and λ is the corner frequency of the low-pass filter. Substituting Eq. (10) into Eq. (9) yields

$$\dot{z} = K_I y. \quad (11)$$

In summary, the entire closed PLL natural frequency tracking system, shown in Fig. 3, is described by Eqs. (12)–(15):

$$\ddot{x} + c\dot{x} + \omega_n^2 x = A \cos \theta, \quad (12)$$

$$\dot{\theta} = \omega_0 + K_{VCO} z, \quad (13)$$

$$\dot{z} = K_I y, \quad (14)$$

$$\dot{y} = \lambda (K_G x \cos \theta - y). \quad (15)$$

3 Analysis Using the Method of Averaging

In order to analyze the transient behavior of the system, the position of the resonator is defined as

$$x := a(t) \cos[\theta(t) + \phi(t)], \quad (16)$$

where $a(t)$ is the amplitude, and $\theta(t) + \phi(t)$ is the instantaneous phase of the resonator position signal, respectively. Since the instantaneous phase of the VCO is equal to θ , the phase difference between the VCO output and the shutter position is equal to ϕ . Differentiating Eq. (16) with respect to time gives the velocity

$$\dot{x} = -a \dot{\theta} \sin(\theta + \phi) + \dot{a} \cos(\theta + \phi) - a \dot{\phi} \sin(\theta + \phi). \quad (17)$$

One of the equations used to determine a and ϕ is obtained by assuming that the sum of the last two terms can be set equal to zero:

$$\dot{a} \cos(\theta + \phi) - a \dot{\phi} \sin(\theta + \phi) = 0. \quad (18)$$

Thus, the velocity equation becomes

$$\dot{x} = -a \dot{\theta} \sin(\theta + \phi). \quad (19)$$

The acceleration is obtained by differentiating Eq. (19) with respect to time,

$$\ddot{x} = -(\dot{a} \dot{\theta} + a \ddot{\theta}) \sin(\theta + \phi) - a \dot{\theta} (\dot{\theta} + \dot{\phi}) \cos(\theta + \phi). \quad (20)$$

Substituting Eqs. (16), (19), and (20) into Eq. (12) yields

$$\begin{aligned} & -(\dot{a} \dot{\theta} + a \ddot{\theta} + c a \dot{\theta}) \sin(\theta + \phi) - a (\dot{\theta}^2 - \omega_n^2 + \dot{\theta} \dot{\phi}) \cos(\theta + \phi) \\ & = A \cos \theta. \end{aligned} \quad (21)$$

Left-multiplying

$$\begin{bmatrix} \dot{\theta} \cos(\theta + \phi) & -\sin(\theta + \phi) \\ \dot{\theta} \sin(\theta + \phi) & \cos(\theta + \phi) \end{bmatrix},$$

which is nonsingular when a trivial condition, $\dot{\theta} \neq 0$, is satisfied, with

$$\begin{bmatrix} (18) \\ (21) \end{bmatrix}$$

yields

$$\begin{aligned} & a (\dot{\theta}^2 - \omega_n^2) \sin(\theta + \phi) \cos(\theta + \phi) + \dot{a} \dot{\theta} + (a \ddot{\theta} + c a \dot{\theta}) \sin^2(\theta + \phi) \\ & = -A \sin(\theta + \phi) \cos \theta, \end{aligned} \quad (22)$$

$$\begin{aligned} & -(a \ddot{\theta} + c a \dot{\theta}) \sin(\theta + \phi) \cos(\theta + \phi) - a \dot{\theta} \dot{\phi} \\ & - a (\dot{\theta}^2 - \omega_n^2) \cos^2(\theta + \phi) = A \cos(\theta + \phi) \cos \theta. \end{aligned} \quad (23)$$

From Eqs. (13) and (14),

$$\ddot{\theta} = K_{VCO} \dot{z} = K_{VCO} K_I y. \quad (24)$$

By substituting Eqs. (24) and (13) into Eqs. (22) and (23), reordering terms, and including Eqs. (14) and (15) yields

$$\begin{aligned} \dot{a} = & -\frac{1}{\omega_0 + K_{VCO} z} \left\{ A \sin(\theta + \phi) \cos \theta \right. \\ & + a [K_{VCO} K_I y + c(\omega_0 + K_{VCO} z)] \sin^2(\theta + \phi) \\ & \left. + a [(\omega_0 + K_{VCO} z)^2 - \omega_n^2] \sin(\theta + \phi) \cos(\theta + \phi) \right\}, \end{aligned} \quad (25)$$

$$\begin{aligned} \dot{\phi} = & -\frac{1}{\omega_0 + K_{VCO} z} \left\{ \frac{A}{a} \cos(\theta + \phi) \cos \theta \right. \\ & + [K_{VCO} K_I y + c(\omega_0 + K_{VCO} z)] \sin(\theta + \phi) \cos(\theta + \phi) \\ & \left. + [(\omega_0 + K_{VCO} z)^2 - \omega_n^2] \cos^2(\theta + \phi) \right\}, \end{aligned} \quad (26)$$

$$\dot{z} = K_I y, \quad (27)$$

$$\dot{y} = \lambda [K_G a \cos(\theta + \phi) \cos \theta - y]. \quad (28)$$

It should be noted that Eqs. (25)–(28) are the exact differential equations describing the evolution of the amplitude and phase of the resonator position, as well as that of the internal states of the low-pass filter and controller. However, these equations are difficult to analyze because they are substantially non-autonomous. The dynamics of the instantaneous phase, θ (Eq. (8)), is a pure integrator. Noting that within a short period of time the variation of $\omega_0 + K_{VCO} z$ is small, the dynamics of the instantaneous phase can be neglected, and it can be regarded as an independent variable, referred to as *normalized time*. Thus, the vector field of the differential equations (25)–(28) can be regarded as an explicit function of time.

As noted before, θ evolves much faster than the other variables, such as a , ϕ , z , and y , and functions $\sin(\theta + \phi)$ and $\cos(\theta + \phi)$ are almost periodic. Within a period of these sinusoidal functions, variables other than θ change very little. Hence, it is possible to apply the averaging method [7,8] to the non-autonomous system described by Eqs. (25)–(28) and approximate it by an autonomous system. M'Closkey and Vakakis [9] investigated an automatic gain control loop, which is used to maintain the oscillation amplitude constant for a microgyroscope, by using the method of averaging. For the single-oscillator simulation case, the averaged and full dynamics were found to be in excellent agreement. A two-oscillator case with small coupling of the sense axis rocking modes was also analyzed, and the effect of coupling on the operation of the automatic gain control loop was shown to be negligible.

As pointed out earlier, θ is regarded as an independent variable and the differential equations (25)–(28) are averaged, with respect to θ , over the interval $[-\pi, \pi]$. The averaged autonomous equations are

$$\dot{\bar{a}} = -\frac{1}{\omega_0 + K_{VCO} \bar{z}} \left\{ \frac{A}{2} \sin \bar{\phi} + \frac{\bar{a}}{2} [K_{VCO} K_I \bar{y} + c(\omega_0 + K_{VCO} \bar{z})] \right\}, \quad (29)$$

$$\dot{\bar{\phi}} = -\frac{1}{\omega_0 + K_{VCO} \bar{z}} \left\{ \frac{A}{2\bar{a}} \cos \bar{\phi} + \frac{1}{2} [(\omega_0 + K_{VCO} \bar{z})^2 - \omega_n^2] \right\}, \quad (30)$$

$$\dot{\bar{z}} = K_I \bar{y}, \quad (31)$$

$$\dot{\bar{y}} = \lambda \left(\frac{K_G}{2} \bar{a} \cos \bar{\phi} - \bar{y} \right), \quad (32)$$

where the bars denote averaged variables. These differential equations describe approximately how the displacement amplitude and phase evolve with time. Although still nonlinear, Eqs. (29)–(32) are easier to analyze than Eqs. (25)–(28).

Since amplitude $a \geq 0$, the equilibrium of the averaged system described by Eqs. (29)–(32) is

Table 1 Numerical values of the parameters used in the simulation

Parameter	Value
A	100 N/kg
K_G	1×10^6 V/m
K_{VCO}	1×10^4 Hz/V
λ	628 rad/s
c	628 1/s
ω_n	6.28×10^4 rad/s

$$\bar{a}_0 = \frac{A}{c\omega_n}, \quad \bar{\phi}_0 = -\frac{\pi}{2},$$

$$\bar{z}_0 = \frac{\omega_n - \omega_0}{K_{VCO}}, \quad \bar{y}_0 = 0,$$

while the oscillating frequency of the resonator and that of the VCO at this equilibrium, $\hat{\theta} = \omega_n$, is the natural frequency of the resonator.

The Jacobian matrix of the nonlinear dynamic system of Eqs. (29)–(32) at equilibrium is

$$\nabla f(\bar{a}_0, \bar{\phi}_0, \bar{z}_0, \bar{y}_0) = \begin{bmatrix} -\frac{c}{2} & 0 & -\frac{AK_{VCO}}{2\omega_n^2} & -\frac{AK_{VCO}K_I}{2c\omega_n^2} \\ 0 & -\frac{c}{2} & -K_{VCO} & 0 \\ 0 & 0 & 0 & K_I \\ 0 & \frac{A\lambda K_G}{2c\omega_n} & 0 & -\lambda \end{bmatrix}, \quad (33)$$

and its characteristic equation is

$$\left(\gamma + \frac{c}{2} \right) \left[\gamma^3 + \left(\lambda + \frac{c}{2} \right) \gamma^2 + \frac{\lambda c}{2} \gamma + \frac{A\lambda K_G K_{VCO} K_I}{2c\omega_n} \right] = 0, \quad (34)$$

where γ is the variable of the characteristic equation. All the eigenvalues of the linearized averaged system are asymptotically stable, if and only if the product of the inner two coefficients is larger than that of the outer two coefficients, i.e.,

$$c \left(\lambda + \frac{c}{2} \right) > \frac{A K_G K_{VCO} K_I}{c \omega_n}. \quad (35)$$

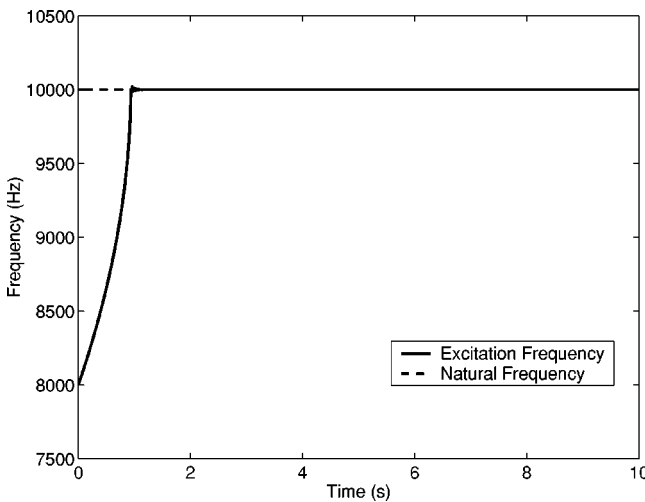


Fig. 4 The excitation frequency tracks the natural frequency when $K_I = 20 < 23.4 = K_{I0}$.

Based on the indirect method of Lyapunov, it is concluded that the equilibrium of the nonlinear averaged system is asymptotically stable within a neighborhood if and only if Eq. (35) is satisfied. For the original exact differential equations, this means that the solution of oscillation at the resonator's natural frequency is stable and attractive, i.e., for some initial excitation at a frequency within a certain range around the resonator's natural frequency, the PLL control system will adjust the excitation frequency to the natural frequency. Equation (35) provides a criterion for selecting the integral control gain, K_I , according to other parameters of the system, such as the hardware gains, K_{VCO} , K_G and A , and the damping factor, c .

4 Simulation Results

The validity of stability criterion (35) was verified by simulating the original exact nonlinear differential equations (12)–(15) for different values of K_I . The numerical values of the parameters used in the simulation are listed in Table I. For these values, the critical value of the integral control gain, K_{I0} , is found to be equal to 23.4. Figures 4 and 5 show how the excitation frequency tracks the natural frequency with $K_I = 20$ and $K_I = 10$, respectively, which are both less than K_{I0} , i.e., the stability criterion (35) is satisfied, while Fig. 6 shows the unstable behavior of the excitation frequency when $K_I = 25 > K_{I0}$. These simulation results demonstrate the validity of the derived criterion for selecting the integral control gain.

Tracking the decaying natural frequency due to fatigue of the spring elements of the resonator was also simulated. It was assumed that the natural frequency decreases exponentially, i.e., $\omega_n = \omega_{n0} e^{-\alpha t}$, with a decay rate $\alpha = 0.01$. A rapid decrease of the natural frequency due to a sudden grain failure is also possible. Figure 7 shows how the excitation frequency tracks the decaying natural frequency for $K_I = 10$. It should be noted that this decay rate is actually much faster than what is expected in fatigue experiments. Preliminary test results have shown that the resonant frequency of a two-beam polysilicon microstructure, such as that shown in Fig. 1 ($50 \mu\text{m}$ beam length with $4 \times 2 \mu\text{m}$ cross-section) decreases by 0.2 kHz after oscillating at resonance with displacement amplitude of $\sim 3 \mu\text{m}$ for 60 h. It can be seen from Fig. 7 that the tracking performance, even for this fast decay, is satisfactory. This simulation result demonstrates the capability of the control system to efficiently track the natural frequency decay in fatigue tests of polycrystalline silicon MEMS devices.

The nonlinearity in the stiffness of the resonator beams was also considered in this study. At resonance, especially in vacuum involving a high quality factor, the oscillation amplitude of the

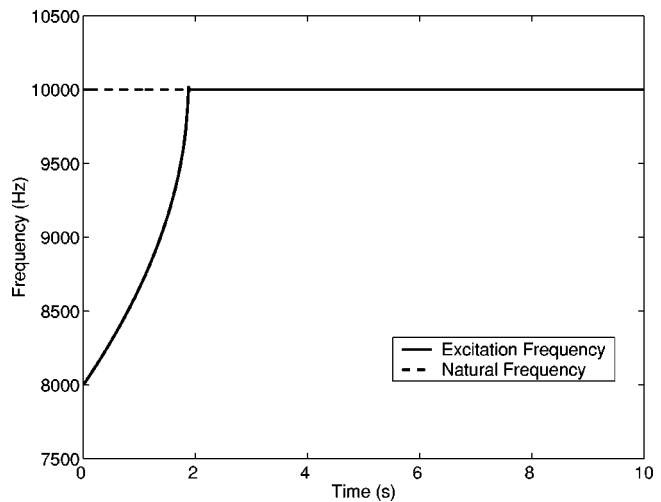


Fig. 5 The excitation frequency tracks the natural frequency when $K_I = 10 < 23.4 = K_{I0}$.

MEMS resonator increases significantly, and a cubic nonlinearity in the stiffness of the suspension beams becomes more significant. The second-order differential equation describing the dynamic behavior of the resonator is modified as

$$\ddot{x} + c\dot{x} + \omega_n^2 x + \beta \omega_n^2 x^3 = A \cos \theta, \quad (36)$$

where β is a coefficient reflecting the relative significance of the cubic nonlinearity. In the simulation for the effect of the stiffness nonlinearity on the control scheme, the quality factor, Q , was increased from 100 to 1000. In correspondence, the normalized viscous damping coefficient, c , decreased from 628 s^{-1} to 62.8 s^{-1} . Two different values of the coefficient β were used in the simulations. First, β was selected such that at the maximum displacement of the shutter, which is equal to $x_0 = QA/\omega_n^2$, the force from the cubic term of Eq. (36) is equal to 1% of the force from the linear term, i.e.,

$$\frac{\beta \omega_n^2 x_0^3}{\omega_n^2 x_0} = 0.01.$$

The simulation result for integral control gain $K_I = 0.1$ is shown in Fig. 8. Figure 8a demonstrates that the PLL controller is still able to bring the excitation frequency to the new resonant frequency

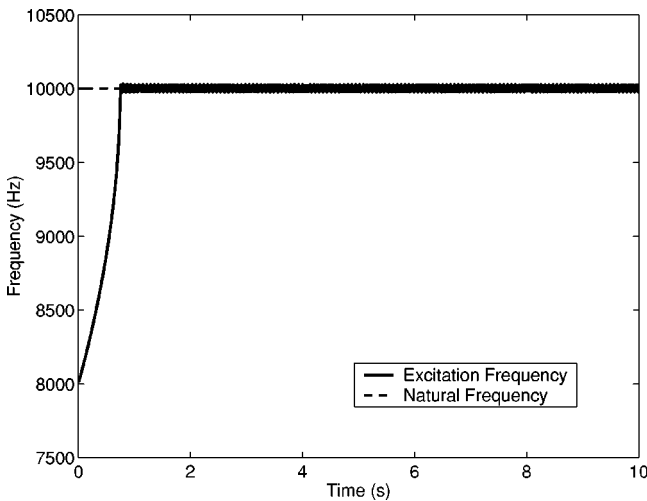


Fig. 6 The excitation frequency oscillates about the natural frequency when $K_I = 25 > 23.4 = K_{I0}$.

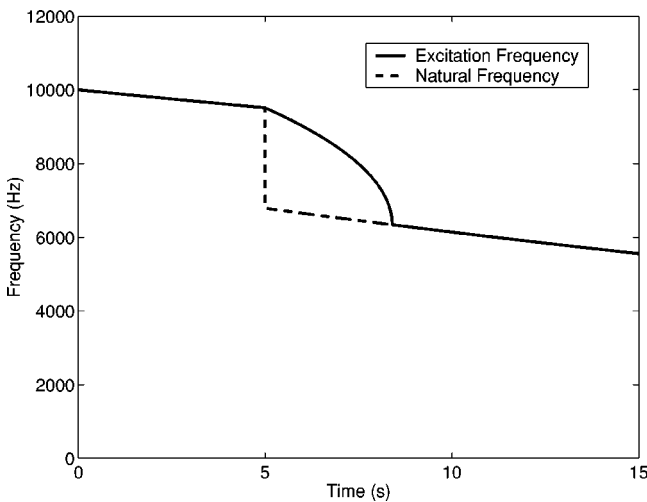


Fig. 7 The excitation frequency tracks the decay of the resonator natural frequency ($K_I = 10$).

that is higher than the nominal natural frequency determined by the linear spring due to the stiffening effect. However, unlike the linear case, the controlled excitation frequency is not constant, as shown in Fig. 8b. The excitation frequency possesses small ripples caused by the abrupt increase and decrease and the hysteresis in the phase-frequency response of the nonlinear resonator. However, the magnitude of the ripples is small and comparable to the resolution of the control scheme, analyzed in detail in the following section. When β is increased such that the force from the cubic term of Eq. (36) is 5% of the force from the linear term, the control scheme fails to track the resonant frequency, as shown in Fig. 9. The unstable behavior of the controlled excitation frequency is a result of the increased hysteresis loop in the phase-frequency response due to the increased nonlinearity.

5 Tracking Resolution

The existence of noise in a control system often degrades its performance and limits its tracking resolution. In MEMS control systems, there are generally two kinds of noise that have to be considered in the analysis of the tracking resolution: a) Brownian noise, which can be modeled as an additive random force with a white spectrum acting on the MEMS resonator, and b) thermal noise in the capacitive position sensing circuits, which is an additive random current in the circuits and can be transformed equivalently as a random position added to the real shutter position. These two kinds of noise are related to the random thermal vibra-

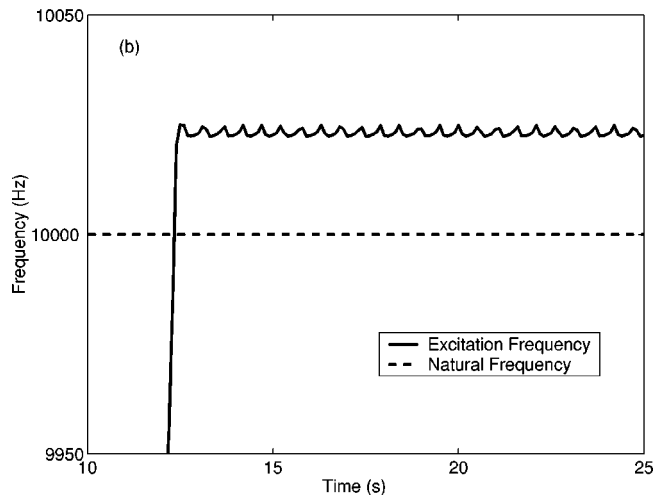
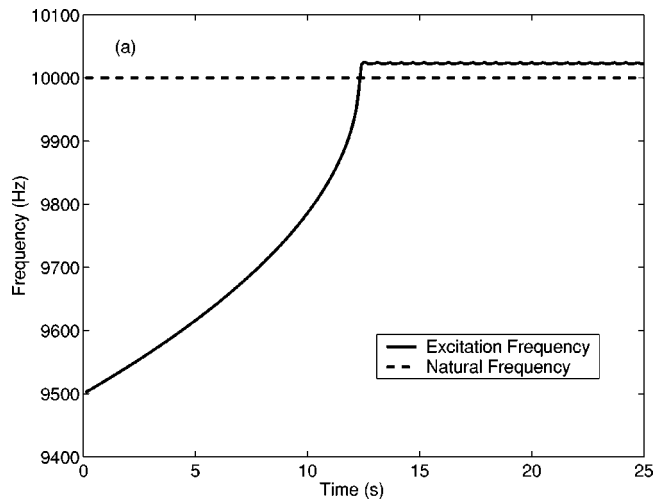


Fig. 8 The response of the excitation frequency for a cubic nonlinear resonator with 1% cubic force ($K_I = 0.1$): a) Overall response, and b) detail at steady state.

tion of particles in materials, such as atoms and electrons, and cannot be eliminated if the operating temperature is above 0 K. The power spectral density (PSD) of Brownian noise [10], S_b , is given by

$$S_b = 4 \frac{k_B T c}{m}, \quad (37)$$

where k_B is the Boltzmann constant, T is the absolute temperature, c is the normalized viscous damping coefficient, and m is the mass of the shutter. The PSD of Brownian noise is a squared normalized force per unit frequency, with units of $N^2/kg^2 \text{ Hz}$. The PSD of the displacement equivalence of the thermal noise [11] in the present capacitive position sensing circuits, S_p , is given by

$$S_p = 4k_B T \left(\frac{2C_0 + C_p}{2V_0 \frac{dC}{d\theta}} \right)^2 R_{\text{wire}}, \quad (38)$$

where C_0 is the nominal sensing capacitance, C_p is the parasitic capacitance, R_{wire} is the wiring resistance, and V_0 is the sensing voltage. The PSD of the position sensing noise is a squared displacement per unit frequency, with units of m^2/Hz . These disturbances limit the achievable tracking accuracy of the control system. The significance of this noise on the tracking effectiveness of the control system is analyzed in this section. The resolution of several MEMS gyroscopes has been investigated in Ref. [12] using these techniques.

Considering the presence of Brownian noise and position sensing noise, differential equations (25)–(28), which govern the control system behavior, were modified as follows:

$$\begin{aligned} \dot{a} = & -\frac{1}{\omega_0 + K_{\text{VCO}}z} \left\{ A \sin(\theta + \phi) \cos\theta + n_b \sin(\theta + \phi) \right. \\ & + a [K_{\text{VCO}}K_I y + c(\omega_0 + K_{\text{VCO}}z)] \sin^2(\theta + \phi) \\ & \left. + a [(\omega_0 + K_{\text{VCO}}z)^2 - \omega_n^2] \sin(\theta + \phi) \cos(\theta + \phi) \right\}, \quad (39) \end{aligned}$$

$$\begin{aligned} \dot{\phi} = & -\frac{1}{\omega_0 + K_{\text{VCO}}z} \left\{ \frac{A}{a} \cos(\theta + \phi) \cos\theta + \frac{n_b}{a} \cos(\theta + \phi) \right. \\ & + [K_{\text{VCO}}K_I y + c(\omega_0 + K_{\text{VCO}}z)] \sin(\theta + \phi) \cos(\theta + \phi) \\ & \left. + [(\omega_0 + K_{\text{VCO}}z)^2 - \omega_n^2] \cos^2(\theta + \phi) \right\}, \quad (40) \end{aligned}$$

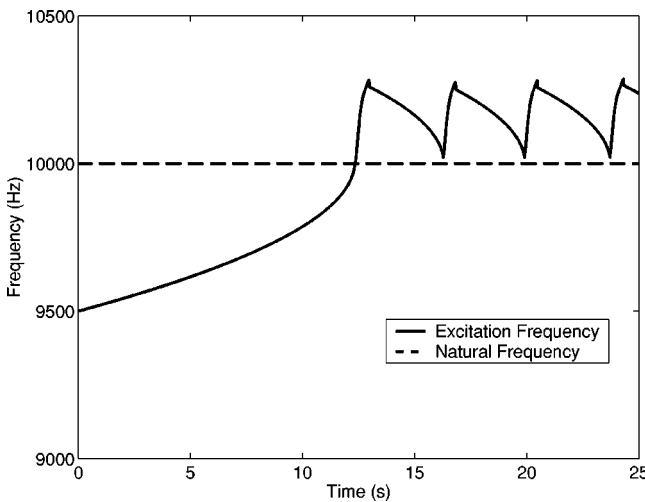


Fig. 9 The response of the excitation frequency for a cubic nonlinear resonator with 5% cubic force ($K_I=0.1$).

$$\dot{z} = K_I y, \quad (41)$$

$$\dot{y} = \lambda [K_A (a \cos(\theta + \phi) + n_p) \cos\theta - y], \quad (42)$$

where n_b and n_p represent Brownian and position sensing noise, respectively, and are white Gaussian noises with mean values equal to 0 and variances σ_b^2 and σ_p^2 , respectively. To simplify the notation in the following analysis, the above equations are written in vector form:

$$\dot{\mathbf{x}} = \mathbf{f}(\mathbf{x}) + \mathbf{g}(\mathbf{x})\mathbf{n}, \quad (43)$$

where

$$\mathbf{x} = \begin{bmatrix} a \\ \phi \\ z \\ y \end{bmatrix}, \quad \mathbf{g}(\mathbf{x}) = \begin{bmatrix} -\frac{\sin(\theta + \phi)}{\omega_0 + K_{\text{VCO}}z} & 0 \\ -\frac{\cos(\theta + \phi)}{a(\omega_0 + K_{\text{VCO}}z)} & 0 \\ 0 & 0 \\ 0 & \lambda K_A \cos\theta \end{bmatrix},$$

$$\mathbf{n} = \begin{bmatrix} n_b \\ n_p \end{bmatrix},$$

and $\mathbf{f}(\mathbf{x}): \mathbb{R} \times S^1 \times \mathbb{R}^2 \rightarrow \mathbb{R} \times S^1 \times \mathbb{R}^2$, where S^1 is the unit circle, is a vector field.

Taking expected values at both sides of Eq. (43),

$$\dot{\bar{\mathbf{x}}} = \bar{\mathbf{f}}(\bar{\mathbf{x}}) + \bar{\mathbf{g}}(\bar{\mathbf{x}})\bar{\mathbf{n}}, \quad (44)$$

where $(\bar{\cdot})$ denotes expected value. The approximate expected values of nonlinear functions $\mathbf{f}(\mathbf{x})$ and $\mathbf{g}(\mathbf{x})$ are obtained by using Taylor series expansion at $\bar{\mathbf{x}}$:

$$\bar{\mathbf{f}}(\mathbf{x}) = \mathbf{f}(\bar{\mathbf{x}}) + \nabla \mathbf{f}|_{\mathbf{x}=\bar{\mathbf{x}}}(\mathbf{x} - \bar{\mathbf{x}}) + O((\mathbf{x} - \bar{\mathbf{x}})^T(\mathbf{x} - \bar{\mathbf{x}})) \approx \mathbf{f}(\bar{\mathbf{x}}), \quad (45)$$

and

$$\bar{\mathbf{g}}(\mathbf{x})\bar{\mathbf{n}} = [\mathbf{g}(\bar{\mathbf{x}}) + \nabla \mathbf{g}|_{\mathbf{x}=\bar{\mathbf{x}}}(\mathbf{x} - \bar{\mathbf{x}}) + O((\mathbf{x} - \bar{\mathbf{x}})^T(\mathbf{x} - \bar{\mathbf{x}}))]\bar{\mathbf{n}} \approx 0. \quad (46)$$

Hence, using the first-order approximation of $\mathbf{f}(\mathbf{x})$ and $\mathbf{g}(\mathbf{x})$, Eq. (45) is simplified as

$$\dot{\bar{\mathbf{x}}} = \bar{\mathbf{f}}(\bar{\mathbf{x}}), \quad (47)$$

which is exactly in the same form as Eqs. (25)–(28). Denoting the averaged functions and variables by $(\bar{\cdot})$, the averaged expected differential equations can be written as

$$\dot{\bar{\mathbf{x}}} = \bar{\mathbf{f}}(\bar{\mathbf{x}}), \quad (48)$$

which is of the same form as Eqs. (29)–(32). Hence, it can be concluded that the averaged expected values of the state variables behave as the averaged state variables in Section 3 without considering the noise.

In order to obtain the tracking resolution, it is necessary to examine the variance propagation of the state variables and the variance of the excitation frequency,

$$\sigma_\omega^2 = \overline{(\omega - \bar{\omega})^2} = \bar{\omega}^2 - \bar{\omega}^2 = K_{\text{VCO}}^2 (\bar{z}^2 - \bar{z}^2) = K_{\text{VCO}}^2 \sigma_z^2. \quad (49)$$

The covariance matrix of the state variables \mathbf{x} is given by

$$P = \overline{(\mathbf{x} - \bar{\mathbf{x}})(\mathbf{x} - \bar{\mathbf{x}})^T} = \overline{\mathbf{x}\mathbf{x}^T} - \bar{\mathbf{x}}\bar{\mathbf{x}}^T, \quad (50)$$

and the time derivative is given by

$$\begin{aligned} \dot{P} &= \frac{d}{dt} (\overline{\mathbf{x}\mathbf{x}^T} - \bar{\mathbf{x}}\bar{\mathbf{x}}^T) \\ &= \overline{f(\mathbf{x})\mathbf{x}^T} + \overline{\mathbf{x}f(\mathbf{x})^T} + \overline{g(\mathbf{x})Sg(\mathbf{x})^T} - \overline{f(\mathbf{x})\bar{\mathbf{x}}^T} - \bar{\mathbf{x}}\overline{f(\mathbf{x})^T}, \quad (51) \end{aligned}$$

where $S = \text{diag}\{\sigma_b^2, \sigma_p^2\}$.

Using Taylor series expansions for $f(\mathbf{x})$ and $g(\mathbf{x})$ at $\bar{\mathbf{x}}$ and taking the first-order approximation yields

$$\underline{\mathbf{x}}f(\mathbf{x})^T + \underline{f(\mathbf{x})}\mathbf{x}^T \approx \underline{\mathbf{x}}f(\bar{\mathbf{x}})^T + \underline{f(\bar{\mathbf{x}})}\mathbf{x}^T + P\nabla f(\bar{\mathbf{x}})^T + \nabla f(\bar{\mathbf{x}})P, \quad (52)$$

and

$$\underline{g(\mathbf{x})Sg(\mathbf{x})}^T \approx g(\bar{\mathbf{x}})Sg(\bar{\mathbf{x}})^T. \quad (53)$$

Let $\bar{A} = \nabla f(\bar{\mathbf{x}})$, then the covariance propagation equation (51) is approximated as

$$\dot{P} = P\bar{A}^T + \bar{A}P + g(\bar{\mathbf{x}})Sg(\bar{\mathbf{x}})^T. \quad (54)$$

Applying averaging to this covariance propagation equation yields

$$\dot{P} = P\bar{A}^T + \bar{A}P + \overline{g(\bar{\mathbf{x}})Sg(\bar{\mathbf{x}})^T}, \quad (55)$$

where \bar{A} is the same as the matrix given by Eq. (33), and

$$\overline{g(\bar{\mathbf{x}})Sg(\bar{\mathbf{x}})^T} = \begin{bmatrix} \frac{\sigma_b^2}{2(\omega_0 + K_{VCO}\bar{z})^2} & 0 & 0 & 0 \\ 0 & \frac{\sigma_b^2}{2a^2(\omega_0 + K_{VCO}\bar{z})^2} & 0 & 0 \\ 0 & 0 & 0 & 0 \\ 0 & 0 & 0 & \frac{\sigma_p^2\lambda^2 K_A^2}{2} \end{bmatrix} =: \bar{W}. \quad (56)$$

Thus, the approximated variance propagation equation is

$$\dot{P} = P\bar{A}^T + \bar{A}P + \bar{W}. \quad (57)$$

The covariance matrix at steady state is the solution to the Lyapunov equation

$$0 = P\bar{A}^T + \bar{A}P + \bar{W}. \quad (58)$$

Using the values from the simulation and solving Eq. (58) numerically, the covariance matrix P and, thus, the standard deviation of the excitation frequency can be obtained as

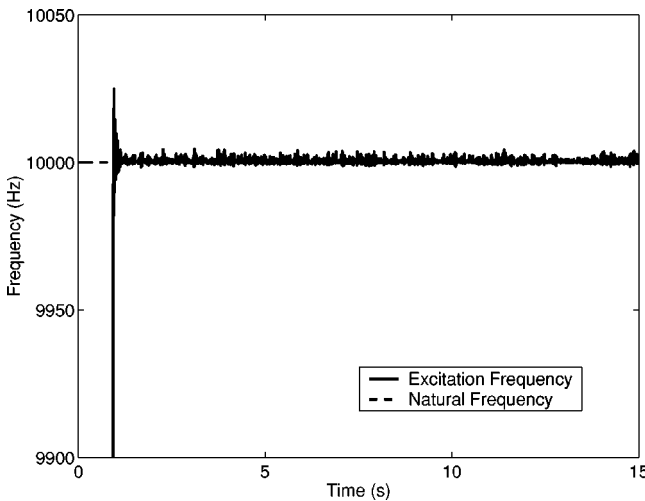


Fig. 10 The excitation frequency tracks the natural frequency under the presence of Brownian and capacitive position sensing noise ($K_f=20$).

$$\sigma_\omega = \sqrt{K_{VCO}^2 P(3,3)} \approx 28 \text{ rad/s}, \quad (59)$$

which corresponds to a standard deviation of ~ 4 Hz in natural frequency. This result is in good agreement with the simulation shown in Fig. 10.

6 Conclusions

A phase-locked loop natural frequency tracking system for a MEMS resonator was presented and the dynamic equations describing this system were analyzed using a method of averaging. A criterion for selecting the control gain was established based on the analysis. The validity of the criterion and effectiveness of the control scheme were verified by simulation results obtained for the control gain satisfying or violating the stability criterion. The performance of the control scheme with a nonlinear resonator was also evaluated in light of simulation results. It was shown that the PLL controller effectively tracks the resonant frequency of a resonator possessing a small cubic nonlinearity, but it fails when the nonlinearity increases further. In addition, the effect of noise on the robustness of the tracking system was considered. The sources of noise include the fundamental Brownian noise and thermal noise in the capacitive position sensing circuits. The tracking resolution under the presence of these two kinds of noise was estimated, and the resolution at steady state was obtained by solving a Lyapunov equation. Both the theoretical estimation and the numerical simulation demonstrated that a sufficiently high resolution could be achieved for the present device. The control scheme described in this paper, together with the necessary driving and sensing circuits, will be implemented in the fatigue experiments of MEMS resonators. Results from these experiments will be presented in future publications.

Acknowledgments

This work was supported in part by Defense Advanced Research Projects Agency (DARPA) under Grant No. DABT63-98-1-0011 and the National Science Foundation (NSF) under Grant No. DMI-9872324. The authors are grateful to the anonymous reviewers for their constructive comments and valuable suggestions.

References

- [1] Komvopoulos, K., 2001, "Microelectromechanical Structures for Multiaxial Fatigue Testing," *Advances in Fracture Research, Proc. of 10th Int. Congress on Fracture*, Elsevier, Honolulu, HI, Paper No. ICF100217OR.
- [2] Markus, K. W., Koester, D. A., Cowen, A., Mahadevan, R., Dhuler, V. R., Roberson, D., and Smith, L., 1995, "MEMS Infrastructure: The Multi-User MEMS Processes (MUMPs)," *Proc. of SPIE: Micromachining and Microfabrication Process Technology*, International Society for Optical Engineering, Austin, TX, **2639**, pp. 54-63.
- [3] Connally, J. A., and Brown, S. B., 1993, "Micromechanical Fatigue Testing," *Exp. Mech.*, **33**(2), pp. 81-90.
- [4] Brown, S. B., Van Arsdell, W., and Muhlstein, C. L., 1997, "Materials Reliability in MEMS Devices," *Proc. of 1997 Int. Conf. on Solid-State Sensors and Actuators*, IEEE, June 16-19, 1997, Chicago, IL, pp. 591-593.
- [5] Dual, J., Mazza, E., Schiltges, G., and Schlums, D., 1997, "Mechanical Properties of Microstructures: Experiments and Theory," *Proc. of SPIE: Microlithography and Metrology in Micromachining III*, Int. Society of Optical Engineering, Austin, TX, **3225**, pp. 12-22.
- [6] Best, R. E., 1999, *Phase-Locked Loops: Theory, Design, and Applications*, 4th Edition, McGraw-Hill, New York, NY.
- [7] Sanders, J. A., and Verhulst, F., 1985, *Averaging Methods in Nonlinear Dynamical Systems*, Springer-Verlag, New York, NY.
- [8] Hale, J. K., 1980, *Ordinary Differential Equations*, 2nd Edition, Krieger, Huntington, NY, pp. 175-212.
- [9] M'Closkey, R. T., and Vakakis, A., 1999, "Analysis of a Microsensor Automatic Gain Control Loop," *Proc. of American Control Conf.*, San Diego, CA, pp. 3307-3311.
- [10] Gabrielson, T. B., 1993, "Mechanical-Thermal Noise in Micromachined Acoustic and Vibration Sensors," *IEEE Trans. Electron Devices*, **40**(5), pp. 903-909.
- [11] Boser, B. E., 1997, "Electronics for Micromachined Inertial Sensors," *Proc. of 1997 Int. Solid-State Sensors and Actuators*, IEEE, June 16-19, 1997, Chicago, IL, pp. 1169-1172.
- [12] Park, S., 2000, "Adaptive Control Strategies for MEMS Gyroscopes," Ph.D. dissertation, Univ. of California at Berkeley.